# 3D Axonal Morphometry of White Matter

**Ali Abdollahzadeh[1], Ilya Belevich[2], Eija Jokitalo[2], Jussi Tohka[1+], and Alejandra Sierra[1*+]**

[1]Biomedical Imaging Unit, A.I.Virtanen Institute for Molecular Sciences, University of Eastern Finland, Kuopio, Finland

[2]Electron Microscopy Unit, Institute of Biotechnology, University of Helsinki, Helsinki, Finland

[*]Corresponding author

[+]These authors contributed equally to this work

## ABSTRACT

Axonal structure underlies white matter functionality and plays a major role in brain connectivity. The current literature on axonal structure is based on the analysis of two-dimensional (2D) cross-sections, which, as we demonstrate, is precarious. We developed a novel pipeline for automated three-dimensional (3D) segmentation and morphometric analysis (ACSON) of the white matter ultrastructure. The automated pipeline eliminates the need for time-consuming manual segmentation of 3D datasets. We applied the pipeline to serial block-face scanning electron microscopy (SBEM) images of the corpus callosum of sham-operated and traumatic brain injury rats (n=1/condition) 5 months after injury. The 3D morphometry showed a substantial variation in axonal diameter along individual axons and the axonal cross-sections were elliptic rather than circular. The axonal diameter was significantly greater in the traumatic brain injured rat, indicating ongoing axonal alterations even at this chronic time-point.

## Introduction

Electron microscopy (EM) techniques are used extensively to assess brain tissue ultrastructure. Studies have reported the morphology, distribution, and interactions of different cellular components in both healthy and pathological brain using transmission electron microscopy (TEM)[1–4]. The ultra-thin sections prepared for TEM can only provide 2-dimensional (2D) information, however, limiting the full characterization of 3-dimensional (3D) cellular structures. Recent advanced EM techniques allow for new possibilities to study the ultrastructure of the brain in 3D[5–9]. One of these techniques is serial block-face scanning electron microscopy (SBEM)[6]. SBEM combines scanning electron microscopy (SEM) with back-scattered electron detection and low beam energies[10]. Images are acquired from the block-face of a sample each time an ultra-microtome inside the vacuum chamber removes the top section from a block-face to expose a new surface for imaging. The result is a stack of high-resolution, high-contrast images of tissue. Compared to other 3D EM techniques, such as focused ion beam (FIB), serial section TEM, or 3D-tomography[5,11], SBEM enables imaging of up to several hundreds of micrometers of tissue at

nanoscopic resolution without manual tissue sectioning. Thus, SBEM is the method of choice for mesoscale imaging of brain tissue ultrastructure.

Despite substantial progress in 3D image acquisition techniques, segmentation and quantification of SBEM data remain challenging. To date, several software tools have been developed that focus on either manual annotation (e.g., KNOSSOS[12], TrakEM2[13], Microscopy Image Browser[14], and CATMAID[15]), or interactive processing of data by combining automated analysis and proof-reading capabilities (e.g., rhoANA[16], ilastik[17], SegEM[18], and ElektroNN[19]). In addition to these software tools, a variety of studies have also proposed segmentation pipelines for analyzing large amounts of TEM data. Recent studies[20–27] initially identified cellular boundaries using pixel-wise classification methods, followed by over-segmentation of the intracellular regions in each 2D image. This procedure requires merging the results within and between consecutive images using different strategies (e.g., watershed merge tree[24], agglomerative or hierarchical clustering[20–22,26,27], and joint segmentation of several images in anisotropic datasets[23,25]).

Although the EM segmentation approaches cited above have yielded impressive results, they have focused on the neuronal reconstruction of grey matter. Here we address quantification of white matter ultrastructure and particularly the morphometry of axons in sham-operated and traumatic brain injured (TBI) animals. Characterization of the white matter ultrastructure is crucial to understanding brain pathology, and in particular, TBI. Such a study will require the segmentation of the white matter components from 3D-SBEM datasets. The previously established segmentation methods do not address the segmentation of white matter for several reasons. First, using manual or semi-automated segmentation software tools (e.g., TrackEM2[13] and ilastik[17]) or pipelines (Chklovskii *et al.*[21]), would be prohibitively time consuming. Providing annotated data, i.e., training data, for supervised learning-based segmentation methods, such as SegEM[18] and ElektroNN[19], is also very time consuming. Second, our interest lies in segmentation of several white matter constituents, such as myelin, myelinated and unmyelinated axons, cell bodies, mitochondria, and vesicles. The methods utilizing binary pixel classifiers[24,25], which assign a pixel as either a cell boundary or a cell-interior, are inappropriate for this type of multiclass segmentation problem. Especially if subcellular structures such as mitochondria are not labeled separately, the clustering step of these methods fails to correctly merge regions within a complete cell[27]. Some studies have addressed the multiple-class problem[23,26,27], and segmented mitochondria as a subcellular structure. These approaches, however, are only valid for grey matter, which lacks myelin. In the SBEM images of white matter, the segmentation of mitochondria in the presence of myelin is extremely difficult because the signal intensity and textural features of mitochondria and myelin are highly similar. Therefore, the segmentation of SBEM images of white matter requires a specifically developed method to address these problems. No prior studies have addressed the automated cross-sectional analysis of axons in grey matter or white matter. Therefore, it is first necessary to design a novel approach to quantify the morphometry of axons.

We developed a novel pipeline (ACSON) for automated 3D segmentation and morphometry of axons in mesoscale SBEM volumes of white matter. The automated pipeline eliminates the need for time-consuming manual segmentation of 3D datasets and enables full 3D analysis of the white matter ultrastructure. ACSON segments the main cellular and subcellular components

of the corpus callosum. To confirm the accuracy of the automated segmentation, the automated segmentation was evaluated against manual annotation by an expert. We quantified the actual cross-sections of the segmented axons based on their diameter, variation, and eccentricity. We analyzed the morphological features of SBEM datasets from the ipsilateral and contralateral sides of the corpus callosum in sham-operated and TBI rats.

## Results

### ACSON segmentation pipeline automatically annotates the white matter ultrastructure

We devised the ACSON segmentation pipeline to annotate the ultrastructure in SBEM volumes of white matter. The segmentation procedure of ACSON labeled white matter voxels as myelin, myelinated and unmyelinated axons, cells, mitochondria, and vesicles. In addition, separate labels were provided for individual axons. The ACSON segmentation pipeline, illustrated in Fig. 1, comprised the following steps: 1) denoising the SBEM volume; 2) segmenting using the bounded volume growing (BVG) technique, which integrates seeded region growing[28] and edge detection algorithms in 3D; 3) refining the segmentation with supervoxel techniques; 4) segmenting the subcellular structure and cells, and annotating myelinated and unmyelinated axons.

### Evaluation of the ACSON segmentation pipeline

Figure 2a illustrates the 3D rendering of myelinated axons and cells (white arrowheads) in the contralateral corpus callosum of the sham-operated rat. The figure depicts the reconstruction of myelinated axons with different thicknesses running along the dataset and organizing bundles with different orientations.

We also quantified the accuracy of the ACSON segmentation pipeline against manual segmentation by an expert. The expert (A.S.) manually segmented three 2D images (images 50, 55, and 60) from the contralateral dataset of the sham-operated rat. The images were selected to be 0.2 µm apart. The expert had no access to the automated segmentations of the dataset. The manual segmentation of a single 2D image required $\sim$ 10 h. Figure 2b shows the manual segmentations and the corresponding images produced by the automated segmentation. The segmentation accuracy was quantified using weighted Dice coefficients (see Materials and Methods). The maximum value for a Dice coefficient is one, which occurs when a segmented region by ACSON perfectly matches a region segmented manually. If no overlap occurs, the Dice coefficient is equal to zero (Supplementary Fig. S2). Note that each axon was considered to be its own region, which is a much more stringent evaluation criterion than considering all axons as a single region. Table 1 reports the weighted Dice coefficient values of the three slices shown in Figure 2b, indicating substantial agreement between the automated and manual segmentations for myelin and myelinated axons.

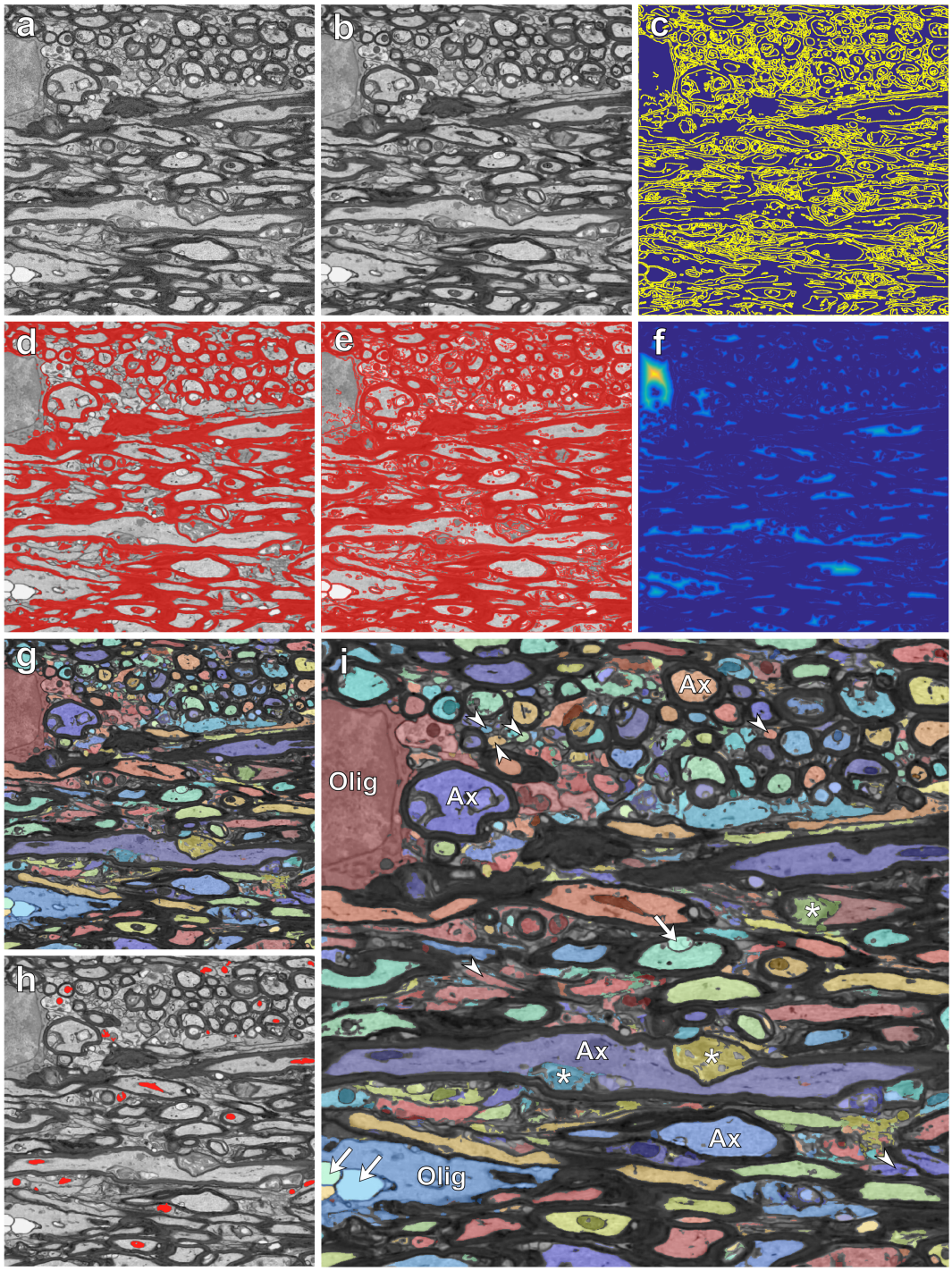


**Figure 1.** White matter ACSON segmentation pipeline. (**a**) A 2D representative image of the SBEM dataset from the contralateral corpus callosum of the sham-operated rat. (**b**) The same image denoised with BM4D. (**c**) Dilated Canny edges of the denoised SBEM dataset. (**d**) Myelin labels obtained with BVG. (**e**) Union of myelin and Canny edges generating a binary mask $B$. (**f**) The Euclidean distance transform was calculated individually for every slice of $B$ to define the location of the seeds for the BVG algorithm. (**g**) The BVG segmentation of all ultrastructures, excluding myelin and mitochondria. (**h**) Cavities of the segmented axons and their refinement with the SLIC supervoxel technique to segment mitochondria. (**i**) ACSON segmentation pipeline annotated the SBEM volumes of the corpus callosum into the intra-axonal space of myelinated axons (Ax), intra-axonal space of unmyelinated axons (white arrowheads), oligodendrocyte cell body and its processes (Olig), mitochondria, vesicles (white arrows), and delamination or pockets in myelin sheaths (asterisk).

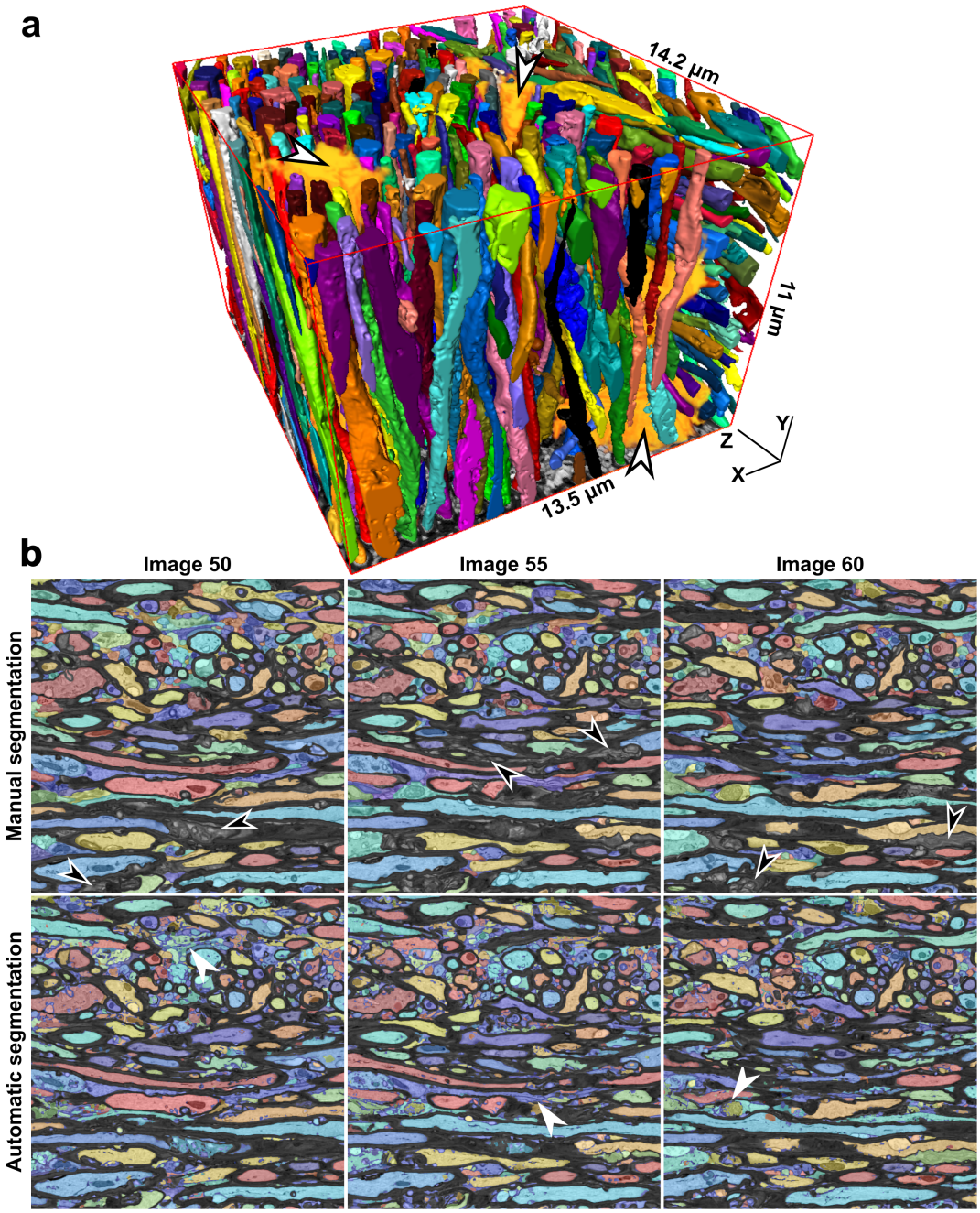


**Figure 2.** (**a**) The 3D reconstruction of myelinated axons and cell processes (white arrowheads) from the contralateral corpus callosum of the sham-operated rat. (**b**) Manual expert segmentation and automated segmentation of three images from the same dataset. The black arrowheads indicate delamination in the myelin sheaths. These substructures were annotated as myelin in the manual annotation, while the automated segmentation excluded the myelin delamination from the myelin-labeled structures. Occasionally, the automated segmentation erroneously merged neighboring unmyelinated axons when the space between the membranes was poorly resolved (white arrowheads). The automated segmentation of myelinated axons was in excellent agreement with the manual segmentation, as shown in Table 1.

**Table 1.** Weighted Dice coefficients of ACSON segmentation compared to manual segmentation, for myelin, myelinated and unmyelinated axons, and for all ultrastructures together. Each axon was considered to be its own region.

| | Image 50 | Image 55 | Image 60 |
|---|---|---|---|
| Myelinated axons | 0.89 | 0.92 | 0.91 |
| Myelin | 0.89 | 0.88 | 0.88 |
| Unmyelinated axons | 0.52 | 0.51 | 0.51 |
| All ultrastructures | 0.77 | 0.77 | 0.78 |

### ACSON morphometry pipeline automatically quantifies the segmented axons

The ACSON morphometry pipeline quantified cross-sections of the intra-axonal space of myelinated and unmyelinated axons. A cross-section is the intersection of a segmented axon and a perpendicular plane to the axonal skeleton. To detect the axonal skeleton, we defined three points in the axon domain: one with the largest distance from the axon surface and two endpoints of the axons, i.e., the tips of the axon. The minimum-cost path connecting these three points was defined as the axonal skeleton (Fig. 3a). The orientation of the cross-sectional planes at each skeleton point was determined by the unit tangent vector at that point. Figure 3a shows the cross-sectional planes at three randomly selected positions along an axon. As Fig. 3a illustrates, for each cross-section we measured the diameter, i.e., minor axis of the fitted ellipses, and eccentricity. Figure 3b shows the cross-sectional diameter along an axon, and shows that the axon diameter is not constant. Note that mitochondria and vesicles are included in the axonal domain.

### 3D morphometry of the ultrastructure of the corpus callosum

We quantified the morphological and volumetric aspects of the white matter ultrastructure in our SBEM datasets. For the morphological analysis, we thresholded axons based on their length, and preserved those axons whose length was long enough to run through the SBEM volumes (Fig. 2a). The thresholding also eliminated subcellular structures that were mistakenly labeled as axons. We defined the threshold for myelinated axons as the mean length of all myelinated axons, which was equal to 10 µm. Similarly, we excluded unmyelinated axons shorter than the mean length of all unmyelinated axons, which was 4 µm.

We subjected the axonal diameters to non-parametric hypothesis testing using the Wilcoxon rank sum test[29] and Kolmogorov-Smirnov test[30,31] (K-S test). The Wilcoxon rank sum test measured the difference between the median of the distributions, and the K-S test measured the distance between the cumulative distribution function of the distributions. We set the alpha-threshold defining the statistical significance as 0.05 for all analyses.

The diameter of myelinated axons was greater on the ipsilateral side than on the contralateral side in both the sham-operated and TBI animals (Fig. 4a, b). In addition, the diameter of myelinated axons was greater in the TBI rat than in the sham-operated rat on both sides of the brain (Fig. 4a, b). We did not detect a significant difference in the diameters of unmyelinated axons between the ipsilateral and contralateral samples in either the sham-operated or TBI animal (Fig. 5a, b). The diameter of

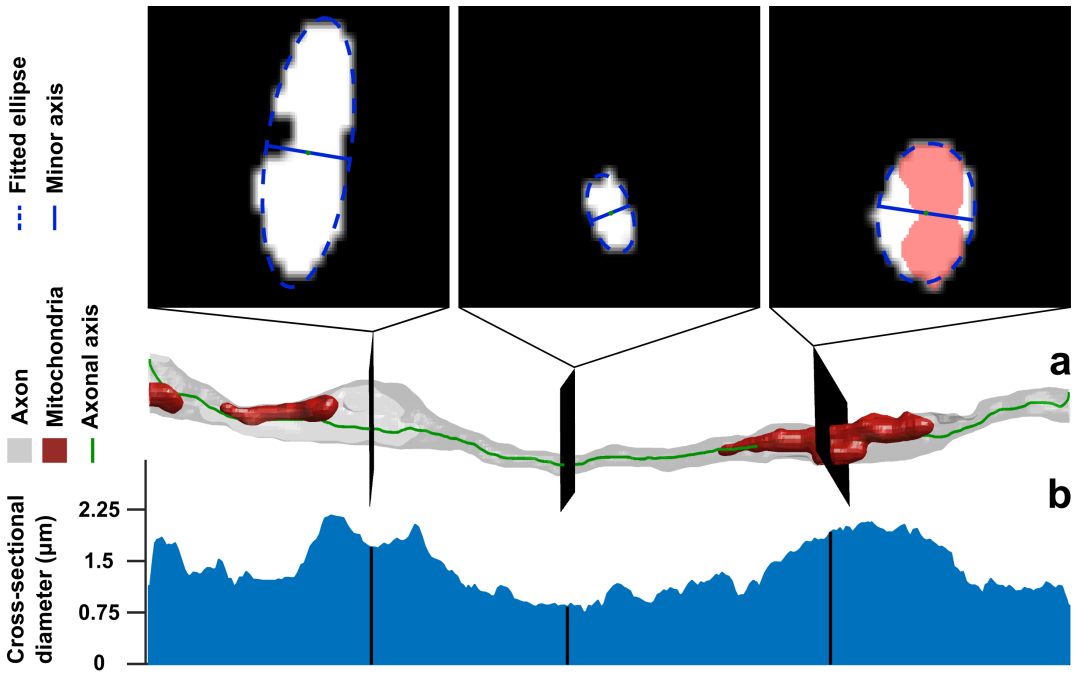


**Figure 3.** ACSON morphometry. (**a**) 3D reconstruction of a representative intra-axonal space of one myelinated axon and its mitochondria. Three intersecting planes at randomly selected positions show the cross-section of the myelinated axon. We defined the cross-sectional diameter as the minor axis of the fitted ellipses. (**b**) The cross-sectional diameter varied along the axon.

unmyelinated axons was greater in the TBI rat compared with the sham-operated rat on both sides of the brain (Fig. 5a, b). Because we obtained a smaller threshold for unmyelinated axons, we also analyzed longer unmyelinated axons. The results were preserved for unmyelinated axons longer than 6 and 7 µm, as shown in Supplementary Fig. S3.

In the same manner, we compared coefficient of variation (CV) and the mean eccentricity of myelinated and unmyelinated axons between datasets. The percentage of the variability of the axonal diameter along an axon is represented by CV. The eccentricity is a measurement of how much a conic section deviates from being circular. For example, the eccentricity of a circle is zero and that of an ellipse is greater than zero but less than one. Table 2 shows the median and median absolute deviation of CV and the mean eccentricity in our datasets. We did not detect significant differences between the sham-operated and TBI datasets. Comparison of myelinated and unmyelinated axons within each dataset, however, revealed that CV and mean eccentricity were significantly greater in unmyelinated axons than in myelinated axons, and both were markedly different from zero. Taken together, these results indicate that the axonal diameter varied along each axon, and the axonal cross-sections were not circular, but elliptical.

We analyzed the relation of the axonal diameter and its standard deviation (SD) along individual axons (Fig. 4c-f and Fig. 5c-f). We first computed the Pearson correlation coefficient ($r$) to determine if a linear relationship existed between these two quantities. The results indicated a significant correlation between the axonal diameter and its SD for both myelinated and unmyelinated axons in all datasets (Fig. 4c-f and Fig. 5c-f). The significance was established with a permutation test in which

the sampling distributions were not assumed to be parametric. We modeled the relations using simple linear regression analysis, and compared the regression slopes using a permutation test. In all datasets, the relation between axonal diameter and its SD had a positive regression slope, indicating that as axonal diameter increased its SD also increased. In myelinated axons, the regression slope was steeper (i.e., the per unit change was greater) in the TBI rat compared with the sham-operated rat on both sides of the brain ($p < 0.01$) (Fig. 4c-f). The analysis did not show significant differences between the contralateral and ipsilateral corpus callosum of the sham-operated or TBI animals. (Fig. 4c-f). The analysis of unmyelinated axons did not show substantial changes in the slope among the datasets (Fig. 5c-f).

We also quantified the volumetric aspects of myelin in our 3D-SBEM datasets. The ultrastructure volumetry was dataset-dependent, preventing a direct cross-comparison between datasets. For example, the volume of cell body/processes varied among datasets, influencing the volume of the other ultrastructures (see the results of volumetric analysis in Supplementary Table S1). Therefore, we calculated the implicit representation of the g-ratio[32] with no measurement of the myelin thickness[33], denoted as $aggregate\ g\text{-}ratio = \sqrt{1 - Myelin^*}$. We defined $Myelin^*$ as the ratio of the myelin volume to the myelin volume plus the intra-axonal volume of all myelinated axons. Assuming that all axons within a SBEM volume have a constant g-ratio, then the aggregate g-ratio is equal to the g-ratio. The aggregate g-ratio for the ipsilateral and contralateral corpus callosum of the sham-operated rat were 0.62 and 0.62, respectively, while those for the ipsilateral and contralateral corpus callosum of the TBI rat were 0.59 and 0.59, respectively. The aggregate g-ratio was slightly smaller in the TBI rat than in the sham-operated rat. The increase in the axonal diameter, together with the decrease in the aggregate g-ratio indicate an increase in myelin thickness [Supplementary section (evaluation of myelin thickness), Supplementary Fig. S4, and Supplementary equation (S1)].

**Table 2.** Analysis of the coefficient of variation (CV) and the mean eccentricity of ipsilateral and contralateral corpus callosum of the sham-operated and TBI rats. The median absolute deviation (MAD) is a robust measure of SD not affected by a few outliers. We did not observe significant difference between sham-operated and TBI datasets. Within datasets, however, all differences between myelinated and unmyelinated axons were significant with $p < 0.001$ according to the Wilcoxon rank sum and K-S tests.

| | | CV (%) | | | | Mean eccentricity | | | |
|---|---|---|---|---|---|---|---|---|---|
| | | Sham | | TBI | | Sham | | TBI | |
| | | ipsi | contra | ipsi | contra | ipsi | contra | ipsi | contra |
| Myelinated axons | Median | 31.80 | 28.29 | 33.00 | 30.20 | 0.69 | 0.71 | 0.67 | 0.67 |
| | MAD | 9.00 | 7.47 | 7.74 | 7.90 | 0.04 | 0.05 | 0.04 | 0.04 |
| Unmyelinated axons | Median | 39.35 | 42.37 | 41.65 | 41.55 | 0.80 | 0.80 | 0.79 | 0.80 |
| | MAD | 11.90 | 9.29 | 11.20 | 9.90 | 0.06 | 0.05 | 0.05 | 0.05 |

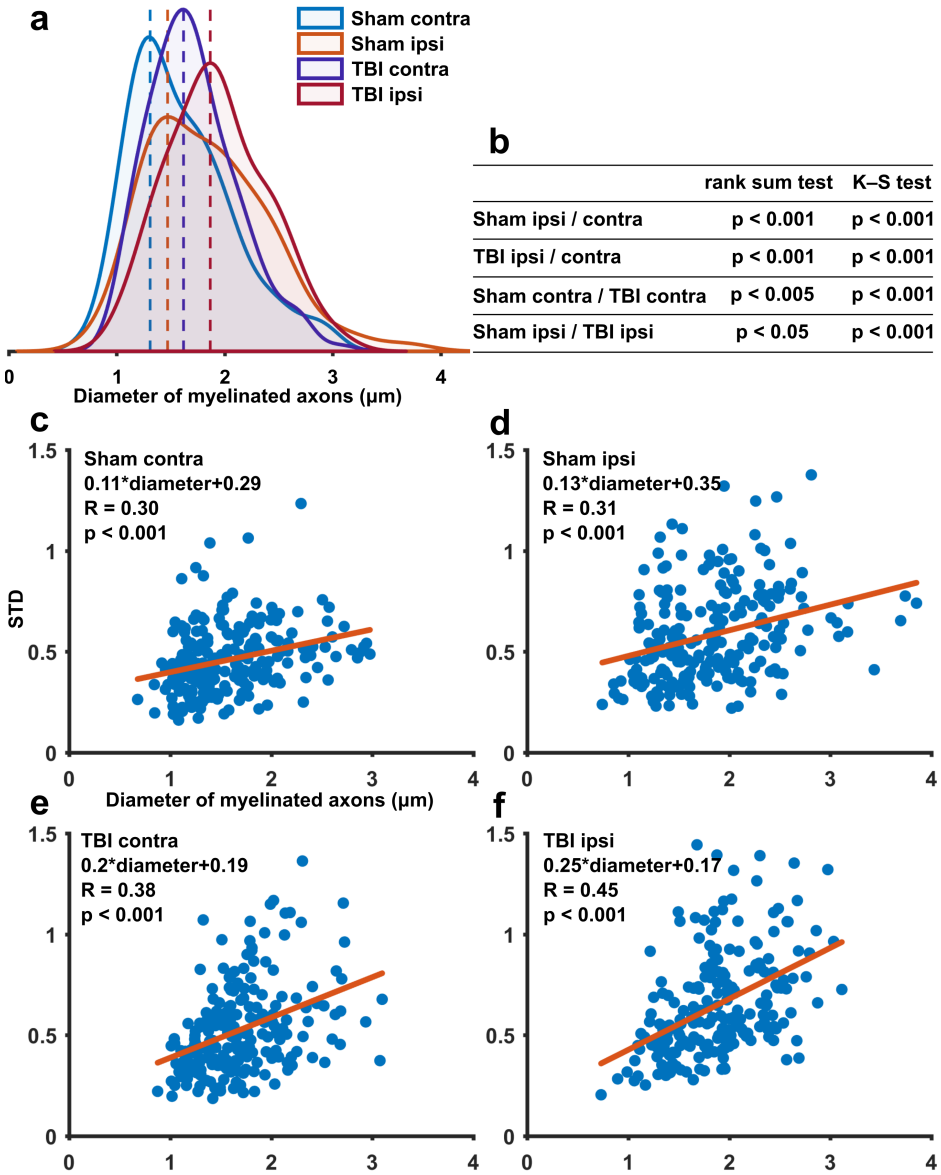


| | rank sum test | K–S test |
|---|---|---|
| Sham ipsi / contra | p < 0.001 | p < 0.001 |
| TBI ipsi / contra | p < 0.001 | p < 0.001 |
| Sham contra / TBI contra | p < 0.005 | p < 0.001 |
| Sham ipsi / TBI ipsi | p < 0.05 | p < 0.001 |

**Figure 4.** Diameter of myelinated axons in ipsilateral and contralateral corpus callosum of sham-operated and TBI rats. (**a**) Diameter of myelinated axons. (**b**) p-values obtained by non-parametric hypothesis testing using the Wilcoxon rank sum test and K-S test. (**c**-**f**) The relation between axonal diameter and its SD in different datasets. A permutation test showed a significant correlation ($R$) between axonal diameter and its SD.

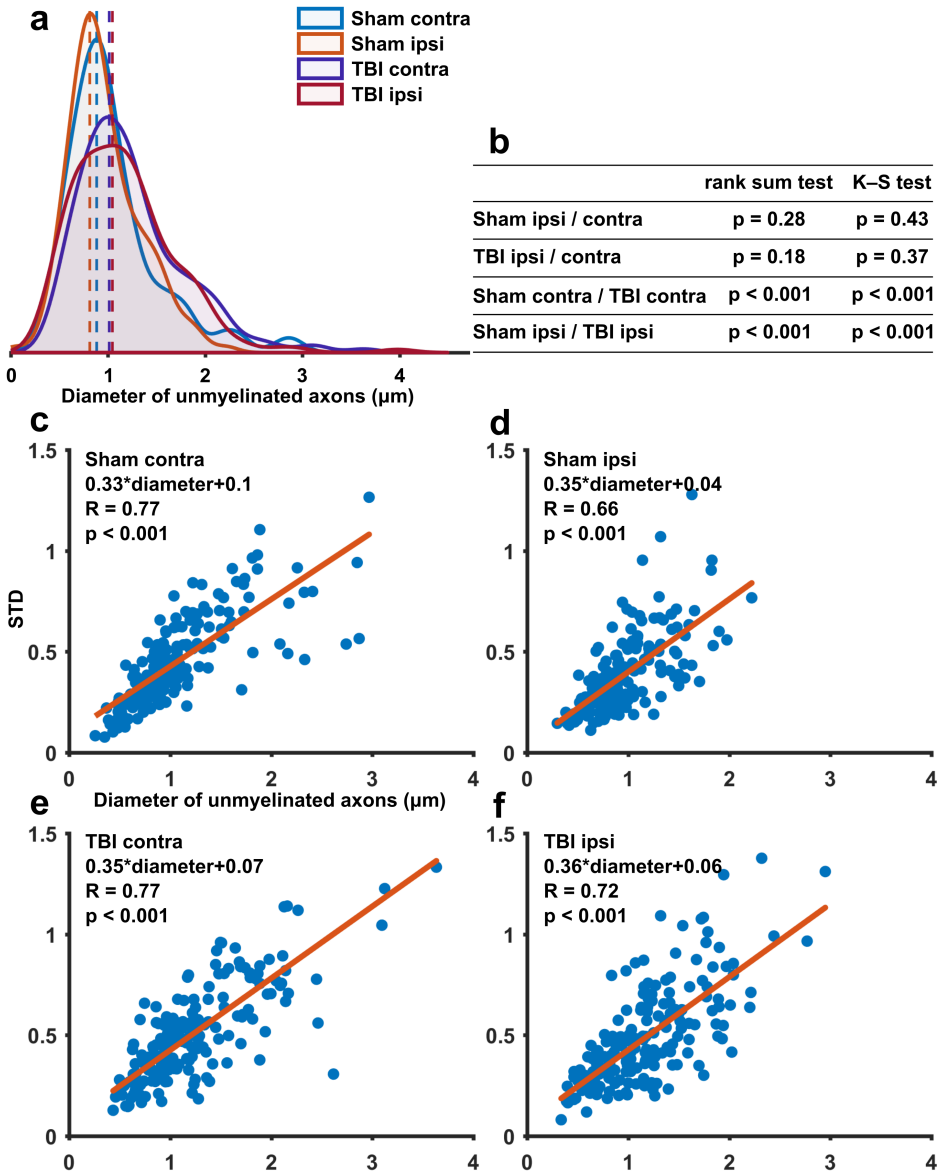


| | rank sum test | K–S test |
|---|---|---|
| Sham ipsi / contra | p = 0.28 | p = 0.43 |
| TBI ipsi / contra | p = 0.18 | p = 0.37 |
| Sham contra / TBI contra | p < 0.001 | p < 0.001 |
| Sham ipsi / TBI ipsi | p < 0.001 | p < 0.001 |

**Figure 5.** Diameter of unmyelinated axons in ipsilateral and contralateral corpus callosum of sham-operated and TBI rats. (**a**) Diameter of unmyelinated axons. (**b**) p-values obtained by non-parametric hypothesis testing using the Wilcoxon rank sum test and K-S test. (**c**-**f**) Analyzing the relation between axonal diameter and its SD in different datasets. A permutation test showed a significant correlation ($R$) between axonal diameter and its SD.

### Computation time

On a 4-core Intel CPU 3.41 GHz machine with 64 GiB RAM, using MATLAB R2016b, the computation times were as follows: block-matching and 4D (BM4D) filtering $\sim$ 5 h, segmentation process $\sim$ 6 h ($\sim$ 0.1 sec/volume), and skeletonization and cross-sectional analysis $\sim$ 6 h. Correcting the segmentation for mitochondria required supervision, which was accomplished in $\sim$ 6 h for the entire SBEM-volume. The manual expert annotation of a single slice of the SBEM datasets required $\sim$ 10 h.

## Discussion

Previous studies that quantified white matter were limited to 2D morphometry, which simplifies the assumptions about axonal morphology. In this paper, we report an extensive 3D morphological analysis of SBEM volumes. For this, we devised a novel pipeline, called ACSON, for automated segmentation and morphometry of the cellular and subcellular components of the corpus callosum in SBEM datasets. ACSON segmented white matter into myelin, the intra-axonal space of myelinated and unmyelinated axons, cell bodies and their processes, and subcellular compartments, such as mitochondria and vesicles. The segmentation accuracy evaluations revealed excellent agreement between the automated and manual segmentation of myelin and myelinated axons. ACSON quantified the morphology of the segmented axons. The 3D morphometry demonstrated a substantial variation in the axonal diameter along each axon, which correlated with its variation. The results indicated that the cross-sections of an axon are more likely to be elliptical than circular. After TBI, we found a significant increase in the diameter of both myelinated and unmyelinated axons, indicating that the alterations persisted for several months after the injury.

Traditionally, studies have represented axons as straight cylinders, and utilized 2D-EM sections to assess the axonal morphology[34–36]. A previous study using serial EM to reconstruct the 3D geometry of unmyelinated axons in peripheral nerves indicated highly irregular axial shapes with periodic varicosities containing organelles[37]. Our study extends the notion of an irregular axonal geometry to both myelinated and unmyelinated axons, raising serious doubts about standard 2D morphometric analysis. First, we found that the axonal axis was not a straight line. Second, we measured substantial variation in axonal diameter along each individual axon. Third, we demonstrated that the cross-sections of axons were most likely to be ellipses rather than circles. Taken together, these findings suggest that 3D analysis of axonal morphometry is required for accurate and unbiased results regarding the axon shape.

Our segmentation and morphometry pipeline is automated. The ACSON-segmentation pipeline requires tuning several parameters, such as the thresholds for measuring similarity or vesicle intensity. These parameters, however, are easy to set. Annotating the mitochondria was the only step that remained a challenge and required human intervention. Compared with manual segmentation, which required $\sim$10 h for a single slice, annotating the mitochondria required $\sim$6 h for the entire dataset comprising 285 SBEM-slices. In an earlier study, Lucchi *et al.*[38] specifically targeted segmentation of mitochondria in high resolution FIB-SEM datasets, i.e., 5-6 nm $\times$ 5-6 nm planar resolution, which is a much finer resolution than in our datasets. They reported that mitochondria and myelin were difficult to discriminate whenever they were in close proximity. The high resolution of their FIB-SEM datasets enabled them to outline the prominent shape-features of mitochondria and they segmented mitochondria almost in the absence of myelin. Unfortunately, their technique is not applicable to our data due to our larger tissue samples, lower resolution, and proximity of mitochondria to myelin.

The ACSON-morphometry pipeline required no user input parameters and extracted a sub-voxel, precise, and naturally smooth axis for each individual axon. We assumed an axon skeleton with no branches and only two endpoints. This allowed us to optimize the computation time for skeleton extraction. The computational efficiency was crucial because we solved the eikonal equation for several thousands of axons with multi-stencils fast marching (MSFM), which is more accurate but

also more time-consuming than the fast marching method (FMM). For the quantification of cross-sections along the axons, we utilized the minor axis of the fitted ellipses as the cross-sectional diameter. Both minor and major axes describe the cross-sections. The major axis, however, is more sensitive to errors in the segmentation and skeletonization steps, whereas the minor axis is more stable and consistent with the actual cross-sectional diameter. As the eccentricity measure is computed using both the minor and major axes, errors in the segmentation and skeletonization steps might have affected the quantification of eccentricity.

The segmentation accuracy evaluation demonstrated substantial agreement between the automated and manual segmentation of myelin and myelinated axons. The weighted Dice coefficients, however, indicated only 50% agreement in the segmentation of unmyelinated axons. There are several possible reasons for the decreased accuracy in the segmentation of unmyelinated axons. First, we specified unlabeled voxels for cell annotation, which was a simplistic assumption. Unlabeled voxels might include other ultrastructures than cells. Second, the delamination or pockets of myelin sheaths were manually annotated as myelin, while the automated segmentation gathered these substructures under the label of unmyelinated axons, and received a Dice coefficient of zero. Finally, the cellular boundaries of unmyelinated axons were often difficult to detect, which resulted in the erroneous merging of neighboring unmyelinated axons.

When analyzing the axonal morphology, we discarded myelinated axons shorter than 10 µm. Axons longer than 10 µm were considered to run along the full length of the SBEM datasets. We obtained a shorter threshold of 4 µm for unmyelinated axons. The main reason for this is that the unmyelinated axons were thinner than myelinated axons, and their diameter along the trajectory could be somewhat lower than the resolution of our datasets. This could lead to erroneous splitting of an unmyelinated axon during segmentation. The threshold was long enough, however, to exclude false positives, and keep the representative length of unmyelinated axons. Increasing the threshold for excluding unmyelinated axons to 6 µm and 7 µm did not change our findings.

It is becoming increasingly clear that white matter pathology plays a major role in brain malfunctions. After TBI, the white matter pathology is extremely complex. The response of an axon to traumatic axonal injury, the damage provoked in axons by the initial mechanical forces and secondary insults[39] can be either degeneration or regeneration. Studies of the white matter ultrastructure indicate axonal swelling in the early stages of TBI[40–42]. Axonal damage persists for years after injury in humans[43] and for up to 1 year in rats[44]. In the present study, we observed morphological changes in the corpus callosum 5 months after severe TBI in rats. We measured an increase in the mean axonal diameter of myelinated axons in the TBI rat as compared with the sham-operated rat. Swelling of the axonal segments might be an indication of ongoing underlying intra-axonal pathology after TBI, such as transport interruption caused by the breakage of microtubules in the cytoskeleton, and accumulation of organelles or vesicles[43,45–47]. This might explain why the regression slope between axonal diameter and its SD was steeper (i.e., the axonal diameter SD increased more for a given increase in axonal diameter) in myelinated axons after TBI. We also found steeper regression slopes for unmyelinated axons compared with the myelinated axons, suggesting that unmyelinated axons are more susceptible to injury[40,48]. Axons can undergo demyelination followed by remyelination.

Our results show an increase in the myelin thickness, which might be indicative of active myelin regeneration. We observed delamination of myelin sheaths more frequently in samples from the TBI animal than in the sham-operated animal.

In addition, we found increased axonal diameter in the contralateral corpus callosum in the TBI rat due to the continuity of this fiber bundle in the brain. Moreover, our data showed an increased diameter of axons in the ipsilateral corpus callosum compared with the contralateral corpus callosum in the sham-operated rat. The sham-operation involved a craniectomy, which might have induced tissue damage that persisted for 5 months after injury. The effect of craniectomy on the tissue ultrastructure is currently unclear.

When characterizing the ultrastructure morphometry, we should note that tissue shrinkage caused by fixation and sectioning might affect quantification of the axon diameter and postmortem tissue volume[49]. In addition, the locations from which the histological specimens were obtained might influence the quantifications. The SBEM datasets in this study were consistently imaged at a specific location in the corpus callosum in both the TBI and sham-operated animals and in both hemispheres. Due to the small tissue size, however, the environment might change from one sample to another. For example, the dataset from the contralateral corpus callosum in the TBI rat contained more cell body/process volume than the other datasets. Thus, studies including more SBEM datasets from several subjects and/or locations in the corpus callosum are necessary to increase the power of our analysis.

## Materials and Methods

### Animal model, tissue preparation, and SBEM imaging

**Animals.** Two adult male Sprague-Dawley rats (10-weeks old, weight 320 and 380g, Harlan Netherlands B.V., Horst, Netherlands) were used in the study. The animals were singly housed in a room (22 $\pm$1 °C, 50% - 60% humidity) with 12 h light/dark cycle and free access to food and water. All animal procedures were approved by the Animal Care and Use Committee of the Provincial Government of Southern Finland and performed according to the guidelines set by the European Community Council Directive 86/609/EEC.

**Traumatic brain injury model.** TBI was induced by lateral fluid percussion injury[50]. Rats were anesthetized with a single intraperitoneal injection (6 mL/kg) of a mixture of sodium pentobarbital (58 mg/kg), magnesium sulphate (127.2 mg/kg), propylene glycol (42.8%), and absolute ethanol (11.6%). A craniectomy (5 mm in diameter) was performed between bregma and lambda on the left convexity (anterior edge 2.0 mm posterior to bregma; lateral edge adjacent to the left lateral ridge). Lateral fluid percussion injury was induced in one rat by a transient fluid pulse impact (21 ms) against the exposed intact dura using a fluid-percussion device (Amscien Instruments, Richmond, VA, USA). The impact pressure was adjusted to 3.1 atm to induce a severe injury. The sham-operated rat underwent all the same surgical procedures except for the impact.

**Tissue processing.** Five months after TBI or sham operation, the rats were transcardially perfused using 0.9% NaCl (30 mL/ min) for 2 min followed by 4% paraformaldehyde ( 30 mL/ min) at 4 °C for 25 min. The brains were removed from the skull and post-fixed in 4% paraformaldehyde /1% glutaraldehyde overnight at 4 °C.

**Tissue preparation for SBEM.** The brains were sectioned into 1-mm thick coronal sections with a vibrating blade microtome (VT1000s, Leica Instruments, Germany). From each brain, a section at approximately 3.80 mm from bregma was selected and two samples from the ipsilateral and the contralateral corpus callosum were further dissected, as shown in Supplementary Fig. S5a. The samples were stained using an enhanced staining protocol[51](see Supplementary Fig. S5b). First, the samples were immersed in 2% paraformaldehyde in 0.15 M cacodylate buffer containing 2 mM calcium chloride (pH = 7.4), and then washed five times for 3 min in cold 0.15 M cacodylate buffer containing 2 mM calcium chloride (pH = 7.4). After washing, the samples were incubated for 1 h on ice in a solution containing 3% potassium ferrocyanide in 0.3 M cacodylate buffer with 4 mM calcium chloride combined with an equal volume of 4% aqueous osmium tetroxide. They were then washed in double distilled $H_2O$ ($ddH_2O$) at room temperature ($5 \times 3$ min). Thereafter, the samples were placed in a solution of 0.01 mg/mL thiocarbohydrazide solution at room temperature for 20 min. The samples were then rinsed again in $ddH_2O$ (5 x 3 min), and placed in 2% osmium tetroxide in $ddH_2O$ at room temperature. Following the second exposure to osmium, the samples were washed in $ddH_2O$ ($5 \times 3$ min), and then incubated in 1% uranyl acetate overnight at 4 °C. The following day, the samples were washed in $ddH_2O$ ($5 \times 3$ min) and *en bloc* Walton's lead aspartate staining was performed. In this step, the samples were incubated in 0.0066 mg/mL lead nitrate in 0.03 M aspartic acid (pH = 5.5) at 60 °C for 30 min, after which the samples were washed in $ddH_2O$ at room temperature ($5 \times 3$ min), and dehydrated using ice-cold solutions of freshly prepared 20%, 50%, 70%, 90%, 100%, and 100% (anhydrous) ethanol for 5 min each, and finally placed in ice-cold anhydrous acetone at room temperature for 10 min. Embedding was performed in Durcupan ACM resin (Electron Microscopy Sciences, Hatfield, PA, USA). First, the samples were placed into 25% Durcupan$^{\#1}$ (without component C):acetone, then into 50% Durcupan$^{\#1}$:acetone, and after into 75% Durcupan$^{\#1}$:acetone overnight. The following day, they were placed in 100% Durcupan$^{\#1}$ for 2 h in a 50 °C oven (2 times), and into 100% Durcupan$^{\#2}$ (4-component mixture) for 2 h in a 50 °C oven. Finally, the samples were embedded in 100% Durcupan$^{\#2}$ in Beem embedding capsules (Electron Microscopy Sciences) and baked in a 60 °C oven for 48 h.

After selecting the area within the samples, as shown in Supplementary Fig. S5c, the blocks were further trimmed into a pyramidal shape with a $1 \times 1$ mm$^2$ base and an approximately $600 \times 600$ µm$^2$ top (face), which assured the stability of the block while being cut in the SBEM microscope. The tissue was exposed on all four sides, bottom, and top of the pyramid. The blocks were then mounted on aluminum specimen pins using conductive silver epoxy (CircuitWorks CW2400). Silver paint (Ted Pella, Redding, CA, USA) was used to electrically ground the exposed block edges to the aluminum pins, except for the block face or the edges of the embedded tissue. The entire surface of the specimen was then sputtered with a thin layer of platinum coating to improve conductivity and reduce charging during the sectioning process.

**SBEM data acquisition.** All SBEM data were acquired on an SEM microscope (Quanta 250 Field Emission Gun; FEI Co., Hillsboro, OR, USA), equipped with the 3View system (Gatan Inc., Pleasanton, CA, USA) using a backscattered electron detector (Gatan Inc.). The top of the mounted block or face was the *x*-*y* plane, and the *z*-direction was the direction of the cutting.

All the samples were imaged with a beam voltage of 2.5 kV and a pressure of 0.15 Torr. The datasets were acquired with a

resolution of 13.8-16.9 nm × 13.8-16.9 nm × 50 nm amounting to an area of 14.1-17.3 µm × 14.1-17.3 µm × 14.25 µm in the $x$, $y$, and $z$ directions, respectively. After imaging, Microscopy Image Browser[14] was used to apply lateral registration to the slices. We quantified the registration using cross correlation analysis between successive slices. Supplementary Fig. S5d shows a representative SBEM volume of the contralateral corpus callosum of the sham-operated rat. We also show two representative images cropped from the sham-operated and TBI volumes in Supplementary Fig. S5e and f, respectively.

### ACSON segmentation pipeline

The ACSON segmentation pipeline annotates the ultrastructure in SBEM volumes of the white matter. The pipeline began with denoising of the SBEM volumes, and proceeded by segmenting the volumes using BVG. The segmented volumes were refined using supervoxel techniques, and, finally, the subcellular structures, cells, and myelinated and unmyelinated axons were annotated.

**Denoising.** SBEM images are degraded by noise from different sources, such as noise in the primary beam, secondary emission noise, and noise in the final detection system[52]. To suppress these complex noise patterns, we applied a non-local BM4D algorithm[53]. Unlike local averaging filters, which smooth an image by averaging values in the neighborhood of a target voxel, non-local filtering considers all the voxels in the image, weighted by how similar these voxels are to the target voxel. BM4D, in particular, enhances a sparse representation in the transform-domain by grouping similar 3D image patches (i.e., continuous 3D blocks of voxels) into 4D data arrays called, groups. The steps to realize the filtering are the 4D transformation of 4D groups, shrinkage of the transform spectrum, and inverse 4D transformation. While BM4D has been extensively used for denoising datasets from diverse imaging modalities, its application in 3D-SBEM datasets is novel. We applied the default parameter values of BM4D for denoising, which automatically estimates the noise type and variance. Figure 1a shows a slice of SBEM volume before filtering, and Fig. 1b illustrates the BM4D output in which the noise has been strongly attenuated.

**Segmentation.** For the segmentation of a 3D-SBEM image, we devised a hybrid technique, named BVG, that integrates seeded region growing and edge detection. To elaborate BVG, we denote a 3D-SBEM image after denoising with BM4D as $z(x) : X \to [0,1]$, where $x \in X$ is a 3D spatial coordinate. Note that the intensity can range from 0 to 1. We defined $\hat{E} \subset X$ as the set of edges of $z$, using a Canny edge detector[54]. We set the parameter values of the Canny edge detector as follows: the SD of the Gaussian filter was $\sqrt{2}$ and thresholds for weak and strong edges were 0.25 and 0.6 times the maximum gradient magnitude. In SBEM volumes with resolution anisotropy and a coarser resolution in the $z$-direction, regions in successive slices did not appear continuously, and areas close to the structure boundaries overlapped. Therefore, we dilated the set of edge coordinates $\hat{E}$ in-plane with a 3×3 square structuring element. The dilated edges are denoted as $E$, and are depicted in Fig. 1c. The edge dilation was proportional to the resolution anisotropy. We then used BVG to segment $z$ into $n+1$ distinct volumes $V_1, V_2, \ldots, V_n, E \subset X$, in which $V_i \cap V_j = \emptyset$, $V_i \cap E = \emptyset$, $\forall i, j = 1, \ldots, n$, $i \neq j$. BVG is a serial segmentation algorithm, meaning that segmentation of $V_i$ starts only when $V_{i-1}$ is segmented. To segment $V_i$, BVG begins with one voxel called the seed, denoted as $S_k \subset V_i$, which iteratively grows—$k$ is the iteration number—and finally results in the volume $V_i$. $N(S_k)$ is in the neighborhood of $S_k$ defined as $N(S_k) = \{r | r \notin S_k, \exists s \in S_k : r \in N(s), r \notin E, r \notin V_{1,\ldots,i-1}\}$, where $N(s)$ is the 3D-neighborhood

of voxel $s$. In each iteration, BVG appends a set of voxels $A$ to $S_k$, where $A = \{x | x \in N(S_k),\ \delta(x) \leq \delta_T\}$ and $\delta(x)$ measures the similarity of voxel $x$ to the set $S_k$. We defined the measure of similarity as $\delta(x) = |z(x) - \frac{1}{|S_k|} \sum_{s \in S_k} z(s)|$ and set the similarity threshold $\delta_T$ to 0.1. An iteration terminates, if $A = \emptyset$, or $|S_k| \geq \vartheta$, where $\vartheta$ is a volume constraint. If $V_i$ grew larger than $\vartheta$, the results were discarded and the voxels within $V_i$ were freed for other regions to compete for them.

The segmentation was initiated by annotating the low-intensity structures, i.e., myelin and mitochondria, which were considered together as $V_1$. BVG was initiated with a random low-intensity voxel $S_1$ with $z(S_1) \leq 0.4$. This one seed was sufficient to segment $V_1$ because myelin is a connected structure in a consecutive SBEM image. We defined $N(s)$ using 26 neighbors, and set $\vartheta = \infty$. Figure 1d shows a slice of the segmented myelin and mitochondria ($V_1$). To segment other structures $V_2, ..., V_n$, we needed a more advanced seeding mechanism. Referring to Fig. 1e, we noticed that other structures are surrounded by myelin and edges. Therefore, we first generated a binary mask, $B$, of the union of the dilated edges $E$ and the myelin-mitochondria segment $V_1$. Denoting each 2D-slice of $B$ as $B_i$, we computed the Euclidean distance transform[55] for every $B_i$ individually, defined as $DT_i$ and shown in Fig. 1f. The pixel value in the distance transform $DT_i$ is the shortest distance from that pixel to a set of pixels $B_i$. We defined the location of the seeds by extracting the regional maxima of each $DT_i$. To segment $V_i$, BVG was initiated with a seed from the set of extracted regional maxima not belonging to any previously segmented $V_j, j = 1, ..., i-1$. We defined $N(s)$ using 6 neighbors and set $\vartheta = 10^6$, which equals 12.5 $\mu m^3$ of tissue or 1.5 times the volume of the largest axons in the dataset. Figure 1g shows one slice of the segmentation of the white matter ultrastructure, not belonging to $B$. The seed extraction overestimates the number of segmented volumes. This does not pose a problem, however, as the serial nature of BVG does not permit repetitive segmentation of an already segmented volume.

**Segmentation post processing.** The segmentation with BVG may result in small volumes with less than 1000 voxels, which may actually belong to larger segments. Therefore, we refined the segmentation by utilizing the SLIC supervoxel[56] technique to attach the small volumes to larger ones. Supervoxels group nearby voxels with similar intensity values into clusters. Particularly, SLIC clusters voxels based on a distance measure defined by $D_s = d_{int} + \frac{c}{\rho} d_{sp}$, where $d_{int}$ ensures intensity similarity and $d_{sp}$ enforces voxel proximity to the supervoxels. In SLIC, the initial supervoxel centers are defined at regular grid steps $\rho$, and their compactness is controlled by $c$. We assigned the SLIC arguments to produce compact and large supervoxels. Thus, we set $c = 25$ and $\rho = 11$ so that each supervoxel contained $\sim$1500 voxels. The large volumes $V_i$ with more than 1000 voxels were refined by the SLIC supervoxels. Supplementary Fig. S1 shows the effect of altering $\rho$ and $c$ while generating supervoxels, and how supervoxels can refine the segmentation. In more detail, suppose that we have generated $Q$ supervoxels $SV_q,\ q = 1, ..., Q$. Then, we re-defined $V_i$ as $V_i' = \bigcup_{q \in I} SV_q$ where $I = \{q' | \frac{|SV_{q'} \cap V_i|}{|SV_{q'}|} \geq 0.2, \forall j < i : \frac{|SV_{q'} \cap V_j|}{|SV_{q'}|} < 0.2\}$. Refining the segmentation with SLIC technique eliminated most of the small volumes by attaching them to the larger segments. Note that as the edges were included in the supervoxels, the supervoxel-based refinement also labeled voxels belonging to the edges.

**Annotating subcellular structures and cells.** The segmentation of myelin sometimes included mitochondria because the boundaries between these two structures were not clearly resolved. We wanted to label mitochondria separately, however, and include them as part of the axons. Not including mitochondria in the axon domain produces cavities, as shown in Fig. 1g. The

cavities can be used to label the mitochondria. To detect the cavities in the axons, on each large volume, $|V_i'| > 10^4$, using a 3D distance transform, we propagated the surface of the volume for 1 µm. The surface of the enlarged volume was then propagated for $-1$ µm shrinking of the volume. Applying this procedure to each large volume altered the morphology of the volume, and closed those cavities smaller than 1 µm. The difference between the altered volume and $V'$ was considered a potential mitochondrion, $M_i$. We refined $M_i$ with SLIC supervoxels with the same parameter values and techniques mentioned in the segmentation post-processing section. Note that because some of the cavities were due to myelin, annotating the mitochondria was finalized using human supervision to check for myelin. Figure 1h shows the final result of the mitochondria segmentation. The myelin segment was then re-defined as the set difference of $V_1$ and all mitochondria, denoted as $MY$. In our SBEM-datasets, vesicles appeared brighter than all of the other ultrastructures. Thus, if $|V_i'| < 2 \times 10^4$ and $\frac{1}{|V_i'|} \sum_{\forall s \in V_i'} z(s) \geq 0.85$, we labeled $V_i'$ as a vesicle. We defined the remaining volumes, not mitochondria nor vesicle, as axons denoted as $AX_i, i = 1, ..., m$. To distinguish if an axon $AX_i$ was a myelinated or unmyelinated axon, we studied the supervoxels intersecting the boundaries of $AX_i$. If these supervoxels contained enough myelin, we considered $AX_i$ to be a myelinated axon. In more detail, let $\Lambda_i$ be the indexes of supervoxels intersecting the boundary of $AX_i$. Now, if $\frac{|(\bigcup_{q \in \Lambda_i} SV_q) \cap MY|}{|(\bigcup_{q \in \Lambda_i} SV_q)|} \geq 0.7$, we considered $AX_i$ to be a myelinated axon.

To label cells and cell-processes, we considered a straightforward approach as the volumes of cells were expected to be larger than the volumes of any other structure, excluding myelin. Recall that we set the volume threshold $\vartheta = 10^6$ for the segmentation of $V_2, ..., V_n$, which leaves some voxels unlabeled. These unlabeled voxels $X'$ comprised cells and cell processes. We segmented $X'$ into $n'$ cells using connected component analysis. In general, we detected 1-2 cell bodies/process in each SBEM-volume. Figure 1i demonstrates the final segmentation results of myelinated axons (Ax), unmyelinated axons (white arrowheads), oligodendrocyte cell body and its processes (Olig), mitochondria, and vesicles (white arrows). Mitochondria and vesicles belonging to axons were colored the same as their corresponding axon. For illustration purposes, we colored the vesicles in the cellular domain different from their corresponding cells.

### ACSON morphometry pipeline

We defined a cross-section as the intersection of a segmented axon $\Omega$ and a perpendicular plane to the axonal skeleton $\gamma$[57]. To detect the axon skeleton $\gamma$ with sub-voxel precision, we adapted a method from Van Uitert & Bitter[58]. First, we defined three points in the axon domain $\Omega$: $x^*$ with the largest distance from the axon surface $\Gamma$, and $x_{e1}$ and $x_{e2}$ as the endpoints of the axons, i.e., the tips of the axon. The minimum-cost path connecting $x_{e1}$ to $x_{e2}$ through $x^*$ was the axon skeleton $\gamma$. The path was found in two steps, first from $x_{e1}$ to $x^*$, and then from $x_{e2}$ to $x^*$. Mathematically,

$$\gamma = \arg\min_P \int_{x_{e1}}^{x_{e2}} H(P(\varsigma)) d\varsigma, \tag{1}$$

where $\varsigma$ traces the path $P$, and $H$ is the cost function. To enforce the minimum-cost path to run at the middle of the object, the cost function $H$ should be higher if the path moves away from the center. Points $x^*$, $x_{e1}$, and $x_{e2}$ and solving equation (1) was defined by solving an eikonal equation on the axonal domain $\Omega$. The eikonal equation is a non-linear partial differential equation defined as a special case of wave propagation in which the front $\Gamma$ advances monotonically with speed $F(x) > 0$. The eikonal equation can be formulated as $|\nabla T(x)|F(x) = 1$, where $T|_\Gamma = 0$. The solution, $T(x)$, is the shortest time needed to travel from $\Gamma$ to any point $x \in \Omega$, with the speed $F(x) > 0$. Although the eikonal equation can be solved with the FMM[59], we used 3D MSFM[60]. MSFM combines multiple stencils and second-order approximation of the directional derivatives over the FMM to improve the accuracy of solving the eikonal equation on Cartesian domains. To find $x^*$, we computed the time-crossing map $T_1(x)$ from the axon interface $\Gamma$ with constant speed $F_1(x) = 1$, $x \in \Omega$. The global maximum of $T_1$, where $T_1(x) \leq T_1(x^*)$, $\forall x \in \Omega$ was defined as $x^*$. To find $x_{e1}, x_{e2}$, and $\gamma$, we calculated a new time-crossing map $T_2(x)$, starting at $x^*$ to every voxel in $\Omega$, with a non-constant speed $F_2(x) = \left(\frac{T_1(x)}{T_1(x^*)}\right)^2$ for $x \in \Omega$. $T_1(x)|_\Gamma = 0$. Using $H(x) = 1 - F_2(x)$ to define the cost ensured that voxels in the middle of the axon were reached prior to the voxels close to $\Gamma$. We defined the furthest point from $x^*$ on the $T_2$ map, i.e., the global maximum of $T_2$, as $x_{e1}$. Similarly, $x_{e2}$ was defined as the furthest point from $x_{e1}$, at the global maximum of the time-crossing map $T_3(x)$, starting from $x_{e1}$ to every voxel in $\Omega$, with speed $F_2(x)$. For both endpoints, we determined the minimum-cost path between $x_{ei}$ and $x^*$, $\gamma_i$, i = 1,2, by backtracking, starting from $x_{ei}$ and progressing along the negative gradient $-\frac{\nabla T_2(x)}{|\nabla T_2(x)|}$ until $x^*$ was reached. $x^*$ is the global minimum of $T_2(x)$, so that we were guaranteed to find it with backtracking. The backtracking procedure can be described by the ordinary differential equation $\frac{d\gamma_i}{d\varsigma} = -\frac{\nabla T_2}{|\nabla T_2|}$, $\gamma_i(\varsigma = 0) = x_{ei}$, where $\varsigma$ traces $\gamma_i$. We used a 4$^{\text{th}}$ order Runge-Kutta scheme, with a 25 nm step size, to solve the ordinary differential equation with sub-voxel accuracy. The axon skeleton was formed as $\gamma = \gamma_1 \cup \gamma_2$. Note that computing the skeleton in this way prevented the skeleton from cutting corners[61]. Figure 3a shows a 3D reconstruction of an axon, its mitochondria, and the extracted skeleton (axonal axis). Note that $x_{e1}$ and $x_{e2}$ defined as the global maxima of $T_2(x)$ and $T_3(x)$, lie on the axon surface $\Gamma$, and not in the center of the axon. The cost function $H$, however, forces the skeleton to immediately move away from the surface $\Gamma$ toward the center. Therefore, we dropped the first 1 µm at both ends of $\gamma$ in our later calculations.

To determine the cross-sectional planes perpendicular to $\gamma$, we formed a moving reference frame of the size 8 µm×8 µm with 50 nm resolution. At each skeleton point $\varsigma$, the unit tangent vector to $\gamma$ was used to define the orientation of the reference frame. The intersection of the reference frame with the axon defined the cross-section of the axon. Finally, we fitted an ellipse to the 2D cross-sections that enabled us to quantify the cross-sectional morphology of the axons and compute the minor axis and eccentricity of the cross-sections. We considered the minor axis of the fitted ellipse to be the cross-sectional diameter (Fig. 3a).

### Weighted Dice coefficient

The Dice coefficient[62] is defined by $Dice\ Coef(A,B) = \frac{2|A \cap B|}{|A| + |B|}$, where $A$ and $B$ are the regions segmented manually and automatically, respectively. The maximum for a Dice coefficient is equal to one occurring when $A$ perfectly matches $B$. If no overlap occurs between $A$ and $B$, the Dice coefficient is equal to zero. Let $A_i, i = 1, ..., a'$, and $B_j, j = 1, ..., b'$ be the regions

in the manual and automated segmentation, respectively. To assign $A_i$ and the best matching $B_j$, we formed a similarity matrix based on Dice coefficients for any possible pair of $A_i$ and $B_j$, where the element $(i, j)$ of the similarity matrix was $Dice\ Coef(A_i, B_j)$. We used the Hungarian algorithm[63,64] to match the regions. We defined the weighted mean of the Dice coefficients as $\sum_{i=1}^{a'} w_i Dice\ Coef(A_i, B_{b(i)})$, where $b(i)$ is the index of the region best matching $A_i$ and the weight $w_i = \frac{|A_i|}{|\sum_{i=1}^{a'} A_i|}$.

## Acknowledgements

This work was supported by the Academy of Finland (J.T. and A.S.), and Biocenter Finland and University of Helsinki (IB, EJ, and SBEM imaging). We would like to thank Maarit Pulkkinen for her help with the animal handling, and Mervi Lindman and Antti Salminen for help preparing the samples for SBEM.

## Author contributions

A.A., J.T., and A.S. conceived the project and designed the study. A.A. implemented the methods and performed the experiments. A.A., J.T., and A.S. analyzed the data. I.B. and E.J. contributed to electron microscopy imaging. A.A., J.T., and A.S. wrote the manuscript. All authors commented on and approved the final manuscript.

## References

1. Guillery, R. W. Light- and electron-microscopical studies of normal and degenerating axons. In *Contemporary Research Methods in Neuroanatomy*, 77–105 (Springer Berlin Heidelberg, Berlin, Heidelberg, 1970). URL http://www.springerlink.com/index/10.1007/978-3-642-85986-1_5. DOI 10.1007/978-3-642-85986-1_5.

2. Wilkins, A. *et al.* Slowly progressive axonal degeneration in a rat model of chronic, nonimmune-mediated demyelination. *J. Neuropathol. & Exp. Neurol.* **69**, 1256–1269 (2010). URL https://academic.oup.com/jnen/article-lookup/doi/10.1097/NEN.0b013e3181ffc317. DOI 10.1097/NEN.0b013e3181ffc317.

3. Lakovic, K. *et al.* Bilirubin and its oxidation products damage brain white matter. *J. Cereb. Blood Flow & Metab.* **34**, 1837–1847 (2014). URL http://journals.sagepub.com/doi/10.1038/jcbfm.2014.154. DOI 10.1038/jcbfm.2014.154.

4. Donovan, V. *et al.* Repeated mild traumatic brain injury results in long-term white-matter disruption. *J. cerebral blood flow metabolism* **34**, 715–723 (2014). URL http://www.ncbi.nlm.nih.gov/pubmed/24473478. DOI 10.1038/jcbfm.2014.6.

5. Torrealba, F. & Carrasco, M. A. A review on electron microscopy and neurotransmitter systems. *Brain Res. Rev.* **47**, 5–17 (2004). DOI 10.1016/j.brainresrev.2004.06.004.

6. Denk, W. & Horstmann, H. Serial block-face scanning electron microscopy to reconstruct three-dimensional tissue nanostructure. *PLoS Biol.* **2** (2004). DOI 10.1371/journal.pbio.0020329.

7. Harris, K. M. *et al.* Uniform serial sectioning for transmission electron microscopy. *J. Neurosci.* **26**, 12101–12103 (2006). URL http://www.jneurosci.org/cgi/doi/10.1523/JNEUROSCI.3994-06.2006. DOI 10.1523/JNEUROSCI.3994-06.2006.

8. Hayworth, K., Kasthuri, N., Schalek, R. & Lichtman, J. Automating the collection of ultrathin serial sections for large volume TEM reconstructions. *Microsc. Microanal.* **12**, 86–87 (2006). URL http://www.journals.cambridge.org/abstract_S1431927606066268. DOI 10.1017/S1431927606066268.

9. Knott, G., Marchman, H., Wall, D. & Lich, B. Serial section scanning electron microscopy of adult brain tissue using focused ion beam milling. *J. Neurosci.* **28**, 2959–2964 (2008). URL http://www.jneurosci.org/cgi/doi/10.1523/JNEUROSCI.3189-07.2008. DOI 10.1523/JNEUROSCI.3189-07.2008.

10. Helmstaedter, M., Briggman, K. L. & Denk, W. 3D structural imaging of the brain with photons and electrons. *Curr. Opin. Neurobiol.* **18**, 633–641 (2008). DOI 10.1016/j.conb.2009.03.005.

11. Briggman, K. L. & Bock, D. D. Volume electron microscopy for neuronal circuit reconstruction. *Curr. Opin. Neurobiol.* **22**, 154–161 (2012). URL http://dx.doi.org/10.1016/j.conb.2011.10.022. DOI 10.1016/j.conb.2011.10.022.

12. Helmstaedter, M., Briggman, K. L. & Denk, W. High-accuracy neurite reconstruction for high-throughput neuroanatomy. *Nat. Neurosci.* **14**, 1081–1088 (2011). URL http://www.nature.com/doifinder/10.1038/nn.2868. DOI 10.1038/nn.2868.

13. Cardona, A. *et al.* TrakEM2 software for neural circuit reconstruction. *PLoS ONE* **7** (2012). DOI 10.1371/journal.pone.0038011.

14. Belevich, I., Joensuu, M., Kumar, D., Vihinen, H. & Jokitalo, E. Microscopy Image Browser: A platform for segmentation and analysis of multidimensional datasets. *PLoS Biol.* **14**, 1–13 (2016). DOI 10.1371/journal.pbio.1002340.

15. Saalfeld, S., Cardona, A., Hartenstein, V. & Tomančák, P. CATMAID: Collaborative annotation toolkit for massive amounts of image data. *Bioinforma.* **25**, 1984–1986 (2009). DOI 10.1093/bioinformatics/btp266.

16. Kaynig, V. *et al.* Large-scale automatic reconstruction of neuronal processes from electron microscopy images. *Med. Image Analysis* **22**, 77–88 (2015). DOI 10.1016/j.media.2015.02.001.

17. Sommer, C., Straehle, C., Ullrich, K. & Hamprecht, F. a. ILASTIK : Interactive learning and segmentation toolkit. *Eighth IEEE Int. Symp. on Biomed. Imaging (ISBI)* 230–233 (2011). DOI 10.1109/ISBI.2011.5872394.

18. Berning, M., Boergens, K. M. & Helmstaedter, M. SegEM: Efficient image analysis for high-resolution connectomics. *Neuron* **87**, 1193–1206 (2015). URL http://dx.doi.org/10.1016/j.neuron.2015.09.003. DOI 10.1016/j.neuron.2015.09.003.

19. Dorkenwald, S. *et al.* Automated synaptic connectivity inference for volume electron microscopy. *Nat. Methods* **14**, 435–442 (2017). URL http://dx.doi.org/10.1038/nmeth.4206. DOI 10.1038/nmeth.4206.

**20.** Andres, B., Köthe, U., Helmstaedter, M., Denk, W. & Hamprecht, F. A. Segmentation of SBFSEM volume data of neural tissue by hierarchical classification. *Lect. Notes Comput. Sci. (including subseries Lect. Notes Artif. Intell. Lect. Notes Bioinformatics)* **5096 LNCS**, 142–152 (2008). DOI 10.1007/978-3-540-69321-5_15.

**21.** Chklovskii, D. B., Vitaladevuni, S. & Scheffer, L. K. Semi-automated reconstruction of neural circuits using electron microscopy. *Curr. Opin. Neurobiol.* **20**, 667–675 (2010). URL http://dx.doi.org/10.1016/j.conb.2010.08.002. DOI 10.1016/j.conb.2010.08.002.

**22.** Jain, V. *et al.* Learning to agglomerate superpixel hierarchies. *Adv. Neural Inf. Process. Syst.* 648–656 (2011). URL http://papers.nips.cc/paper/4249-learning-to-agglomerate-superpixel-hierarchies.

**23.** Vazquez-Reina, A. *et al.* Segmentation fusion for connectomics. *Proc. IEEE Int. Conf. on Comput. Vis.* 177–184 (2011). DOI 10.1109/ICCV.2011.6126240.

**24.** Liu, T., Jurrus, E., Seyedhosseini, M., Ellisman, M. & Tasdizen, T. Watershed merge tree classification for electron microscopy image segmentation. In *Pattern Recognition (ICPR), 2012 21st International Conference on*, Icpr (2012). URL http://ieeexplore.ieee.org/xpls/abs_all.jsp?arnumber=6460090. DOI 10.1097/MPG.0b013e3181a15ae8.Screening.

**25.** Funke, J., Andres, B., Hamprecht, F. A., Cardona, A. & Cook, M. Efficient automatic 3D-reconstruction of branching neurons from em data. *Proc. IEEE Comput. Soc. Conf. on Comput. Vis. Pattern Recognit.* 1004–1011 (2012). DOI 10.1109/CVPR.2012.6247777.

**26.** Nunez-Iglesias, J., Kennedy, R., Parag, T., Shi, J. & Chklovskii, D. B. Machine learning of hierarchical clustering to segment 2D and 3D images. *PLoS ONE* **8** (2013). DOI 10.1371/journal.pone.0071715.

**27.** Parag, T., Chakraborty, A., Plaza, S. & Scheffer, L. A context-aware delayed agglomeration framework for electron microscopy segmentation. *PLoS ONE* **10**, 1–19 (2015). DOI 10.1371/journal.pone.0125825.

**28.** Adams, R. & Bischof, L. Seeded region growing. *IEEE Transactions on Pattern Analysis Mach. Intell.* **16**, 641–647 (1994).

**29.** Wilcoxon, F. Individual comparisons by ranking methods. *Biom. Bull.* **1**, 80 (1945). URL http://www.jstor.org/stable/10.2307/3001968?origin=crossref. DOI 10.2307/3001968.

**30.** Kolmogorov, A. N. Sulla determinazione empirica di una legge di distribuzione. *Giornale dell'Istituto Italiano degli Attuari* **4**, 83–91 (1933).

**31.** Smirnov, N. Table for estimating the goodness of fit of empirical distributions. *The Annals Math. Stat.* **19**, 279–281 (1948). URL http://projecteuclid.org/euclid.aoms/1177730256. DOI 10.1214/aoms/1177730256.

**32.** Rushton, W. A. H. A theory of the effects of fiber size in medullated nerve. *The J. Physiol.* 101–122 (1951).

**33.** Stikov, N. *et al.* In vivo histology of the myelin g-ratio with magnetic resonance imaging. *NeuroImage* **118**, 397–405 (2015). URL http://dx.doi.org/10.1016/j.neuroimage.2015.05.023. DOI 10.1016/j.neuroimage.2015.05.023.

**34.** Barazany, D., Basser, P. J. & Assaf, Y. In vivo measurement of axon diameter distribution in the corpus callosum of rat brain. *Brain* **132**, 1210–1220 (2009). DOI 10.1093/brain/awp042.

**35.** Liewald, D., Miller, R., Logothetis, N., Wagner, H. J. & Schüz, A. Distribution of axon diameters in cortical white matter: an electron-microscopic study on three human brains and a macaque. *Biol. Cybern.* **108**, 541–557 (2014). DOI 10.1007/s00422-014-0626-2.

**36.** Stikov, N. *et al.* Quantitative analysis of the myelin g-ratio from electron microscopy images of the macaque corpus callosum. *Data Brief* **4**, 368–373 (2015). DOI 10.1016/j.dib.2015.05.019.

**37.** Greenberg, M. M., Leitao, C., Trogadis, J. & Stevens, J. K. Irregular geometries in normal unmyelinated axons: A 3D serial EM analysis. *J. Neurocytol.* **19**, 978–988 (1990). URL http://link.springer.com/10.1007/BF01186825. DOI 10.1007/BF01186825.

**38.** Lucchi, A., Smith, K., Achanta, R., Knott, G. & Fua, P. Supervoxel-based segmentation of mitochondria in em image stacks with learned shape features. *IEEE Transactions on Med. Imaging* **31**, 474–486 (2012). DOI 10.1109/TMI.2011.2171705.

**39.** Armstrong, R. C., Mierzwa, A. J., Marion, C. M. & Sullivan, G. M. White matter involvement after TBI: Clues to axon and myelin repair capacity. *Exp. Neurol.* **275**, 328–333 (2016). URL http://dx.doi.org/10.1016/j.expneurol.2015.02.011. DOI 10.1016/j.expneurol.2015.02.011.

**40.** Reeves, T. M., Phillips, L. L. & Povlishock, J. T. Myelinated and unmyelinated axons of the corpus callosum differ in vulnerability and functional recovery following traumatic brain injury. *Exp. Neurol.* **196**, 126–137 (2005). DOI 10.1016/j.expneurol.2005.07.014.

**41.** Dikranian, K. *et al.* Mild traumatic brain injury to the infant mouse causes robust white matter axonal degeneration which precedes apoptotic death of cortical and thalamic neurons. *Exp. Neurol.* **211**, 551–560 (2008). DOI 10.1016/j.expneurol.2008.03.012.

**42.** Mierzwa, A. J., Marion, C. M., Sullivan, G. M., McDaniel, D. P. & Armstrong, R. C. Components of myelin damage and repair in the progression of white matter pathology after mild traumatic brain injury. *J Neuropathol Exp Neurol* **74**, 218–232 (2015). URL http://www.ncbi.nlm.nih.gov/pubmed/25668562. DOI 10.1097/NEN.0000000000000165.

**43.** Johnson, V. E., Stewart, W. & Smith, D. H. Axonal pathology in traumatic brain injury. *Exp. Neurol.* **246**, 35–43 (2013). URL http://dx.doi.org/10.1016/j.expneurol.2012.01.013. DOI 10.1016/j.expneurol.2012.01.013.

**44.** Rodriguez-Paez, A. C., Brunschwig, J. P. & Bramlett, H. M. Light and electron microscopic assessment of progressive atrophy following moderate traumatic brain injury in the rat. *Acta Neuropathol.* **109**, 603–616 (2005). DOI 10.1007/s00401-005-1010-z.

**45.** Tang-Schomer, M. D., Patel, A. R., Baas, P. W. & Smith, D. H. Mechanical breaking of microtubules in axons during dynamic stretch injury underlies delayed elasticity, microtubule disassembly, and axon degeneration. *FASEB journal : official publication Fed. Am. Soc. for Exp. Biol.* **24**, 1401–10 (2010). URL http://www.ncbi.nlm.nih.gov/pubmed/20019243http://www.pubmedcentral.nih.gov/articlerender.fcgi?artid=PMC2879950. DOI 10.1096/fj.09-142844.

**46.** Tang-Schomer, M. D., Johnson, V. E., Baas, P. W., Stewart, W. & Smith, D. H. Partial interruption of axonal transport due to microtubule breakage accounts for the formation of periodic varicosities after traumatic axonal injury. *Exp. Neurol.* **233**, 364–372 (2012). URL http://dx.doi.org/10.1016/j.expneurol.2011.10.030. DOI 10.1016/j.expneurol.2011.10.030.

**47.** Hånell, A., Greer, J. E., McGinn, M. J. & Povlishock, J. T. Traumatic brain injury-induced axonal phenotypes react differently to treatment. *Acta Neuropathol.* **129**, 317–332 (2015). DOI 10.1007/s00401-014-1376-x.

**48.** Reeves, T. M., Phillips, L. L., Lee, N. N. & Povlishock, J. T. Preferential neuroprotective effect of tacrolimus (FK506) on unmyelinated axons following traumatic brain injury. *Brain Res.* **1154**, 225–236 (2007). DOI 10.1016/j.brainres.2007.04.002.

**49.** Virtanen, J., Uusitalo, H., Palkama, A. & Kaufman, H. The effect of fixation on corneal endothelial cell dimensions and morphology in scanning electron microscopy. *Acta ophthalmologica* **62**, 577–85 (1984). URL http://www.ncbi.nlm.nih.gov/pubmed/6435388.

**50.** Kharatishvili, I., Nissinen, J. P., McIntosh, T. K. & Pitkänen, A. A model of posttraumatic epilepsy induced by lateral fluid-percussion brain injury in rats. *Neurosci.* **140**, 685–697 (2006). DOI 10.1016/j.neuroscience.2006.03.012.

**51.** Deerinck, T. *et al.* Enhancing serial block-face scanning electron microscopy to enable high resolution 3-D nanohistology of cells and tissues. *Microsc. Microanal.* **16**, 1138–1139 (2010). DOI 10.1017/S14319276100.

**52.** Sim, K. S., Thong, J. T. L. & Phang, J. C. H. Effect of shot noise and secondary emission noise in scanning electron microscope images. *Scanning* **26**, 36–40 (2006). URL http://onlinelibrary.wiley.com/doi/10.1002/sca.4950260106/abstract%5Cnhttp://doi.wiley.com/10.1002/sca.4950260106. DOI 10.1002/sca.4950260106.

**53.** Maggioni, M., Katkovnik, V., Egiazarian, K. & Foi, A. Nonlocal transform-domain filter for volumetric data denoising and reconstruction. *IEEE Transactions on Image Process.* **22**, 119–133 (2013). DOI 10.1109/TIP.2012.2210725.

**54.** Canny, J. A computational approach to edge detection. *IEEE Transactions on Pattern Analysis Mach. Intell.* **PAMI-8**, 679–698 (1986). DOI 10.1109/TPAMI.1986.4767851.

**55.** Rosenfeld, A. & Pfaltz, J. L. Sequential operations in digital picture processing. *J. ACM* **13**, 471–494 (1966). URL http://portal.acm.org/citation.cfm?doid=321356.321357. DOI 10.1145/321356.321357.

**56.** Achanta, R. *et al.* SLIC superpixels. *EPFL Tech. Rep.* **149300**.

**57.** Blum, H. A transformation for extracting new descriptors of shape. *Model. for perception speech visual form* **19**, 362–380 (1967). URL papers2://publication/uuid/33A7D570-B63C-4E43-996A-4DE15D8EE75F.

**58.** Van Uitert, R. & Bitter, I. Subvoxel precise skeletons of volumetric data based on fast marching methods. *Med. physics* **34**, 627–638 (2007). DOI 10.1118/1.2409238.

**59.** Sethian, J. A. A fast marching level set method for monotonically advancing fronts. *Proc. Natl. Acad. Sci.* **93**, 1591–1595 (1996). URL http://www.pnas.org/cgi/doi/10.1073/pnas.93.4.1591. DOI 10.1073/pnas.93.4.1591.

**60.** Hassouna, M. S. & Farag, A. A. Multistencils fast marching methods: A highly accurate solution to the Eikonal equation on Cartesian domains. *IEEE Transactions on Pattern Analysis Mach. Intell.* **29**, 1563–1574 (2007). DOI 10.1109/TPAMI.2007.1154.

**61.** van Heekeren, R. J., Faas, F. G. a. & van Vliet, L. J. Finding the minimum-cost path without cutting corners. *Image Analysis: 15th Scand. Conf. SCIA 2007, Aalborg, Denmark* 263–272 (2007). URL http://link.springer.com/10.1007/978-3-540-73040-8_27. DOI 10.1007/978-3-540-73040-8_27.

**62.** Dice, L. R. Measures of the amount of ecologic association between species. *Ecol.* **26**, 297–302 (1945). URL http://doi.wiley.com/10.2307/1932409. DOI 10.2307/1932409.

**63.** Kuhn, W., Harold. The Hungarian method for the assignment problem. In M, J. (ed.) *50 Years of Integer Programming 1958-2008: From the Early Years to the State-of-the-Art* (Springer, Berlin, Heidelberg, 2010). DOI 10.1007/978-3-540-68279-0.

**64.** Hodneland, E. *et al.* A unified framework for automated 3-D segmentation of surface-stained living cells and a comprehensive segmentation evaluation. *IEEE Transactions on Med. Imaging* **28**, 720–738 (2009). DOI 10.1109/TMI.2008.2011522.